

# A novel multi-frequency technique for the detection of point sources in Cosmic Microwave Background maps

D. Herranz<sup>1\*</sup>, M. López-Caniego<sup>2</sup>, J. L. Sanz<sup>1,3</sup> and J. González-Nuevo<sup>4</sup>

<sup>1</sup> *Instituto de Física de Cantabria, CSIC-UC, Av. los Castros s/n, Santander, 39005, Spain*

<sup>2</sup> *Astrophysics Group, Cavendish Laboratory, J.J. Thomson Avenue, CB9 0E1, Cambridge, United Kingdom*

<sup>3</sup> *CNR Istituto di Scienza e Tecnologie dell'Informazione, via G. Moruzzi 1, I-56124, Pisa, Italy*

<sup>4</sup> *SISSA-I.S.A.S., via Beirut 4, I-34014 Trieste, Italy*

Received –, Accepted –

## ABSTRACT

In this work we address the problem of simultaneous multi-frequency detection of extragalactic point sources in maps of the Cosmic Microwave Background. We apply a new linear filtering technique, the so called ‘matched matrix filters’, that incorporates full spatial information, including the cross-correlation among channels, without making any a priori assumption about the spectral behaviour of the sources. A substantial reduction of the background is achieved thanks to the optimal combination of filtered maps. We describe in detail the new technique and we apply it to the detection/estimation of radio sources in realistic all-sky *Planck* simulations at 30, 44, 70 and 100 GHz. Then we compare the results with the mono-frequencial approach based on the standard matched filter, in terms of reliability, completeness and flux accuracy of the resulting point source catalogs. The new filters outperform the standard matched filters for all these indexes at 30, 44 and 70 GHz, whereas at 100 GHz both kind of filters have a similar performance. We find a noticeable increment of the number of true detections for a fixed reliability level. In particular, for a 95% reliability we practically double the number of detections at 30, 44 and 70 GHz.

**Key words:** methods: data analysis – techniques: image processing – radio continuum: galaxies – cosmic microwave background – surveys

## 1 INTRODUCTION

From the search of extrasolar planets to the study of active galactic nuclei, one of the most common task in all the branches of Astronomy is the detection of faint pointlike objects. Such objects have angular sizes that are smaller than the angular resolution of the telescopes that are used to observe them, and therefore they are usually referred to as *point sources*.

A case of particular interest is the detection of extragalactic point sources (EPS) in maps of the Cosmic Microwave Background (CMB). EPS are known to be a relevant source of contamination for CMB studies, specially at small angular scales, where they hamper the estimation of CMB angular power spectrum both in temperature (Toffolatti et al. 1998; de Zotti et al. 1999; Hobson et al. 1999; de Zotti et al. 2005) and in polarization (Tucci et al. 2004, 2005). Therefore, for the sake of CMB analysis it is

necessary to detect and remove as many extragalactic point sources as possible.

Moreover, in the frequency range spanned by CMB experiments the properties of EPS are poorly studied. Only very recently the *Wilkinson Microwave Anisotropy Probe* (WMAP) satellite (Bennett et al. 2003) has permitted the obtention of the first all-sky complete point source catalogs above  $\sim 0.8$ –1 Jy in the 23–94 GHz range of frequencies (Bennett et al. 2003; Hinshaw et al. 2007; López-Caniego et al. 2007; Chen & Wright 2007; Wright et al. 2008). The upcoming *Planck* mission (Tauber 2005) will allow us to extend these catalogs down to lower flux limits and up to 857 GHz. There is interesting physics to be probed in this frequency range. The new EPS catalogs provided by next generation CMB experiments will not only allow us to follow the behaviour of source counts from existing catalogs to microwave frequencies, but also to study source variability and to discover rare objects such as inverted spectrum radio sources, extreme gigahertz peaked spectrum (GPS) sources and high-redshift dusty galaxies (see for example the *Planck Blue-*

\* E-mail: herranz@ifca.unican.es

book (The Planck Collaboration 2006) for a brief, yet comprehensive review of the rich phenomenology of EPS at microwave frequencies). Thus, the task of detecting point sources is important not only from the point of view of CMB science but also from the point of view of extragalactic Astronomy as well.

Let us consider a single image taken at a given wavelength. Then the problem consists on how to detect a number of objects, all of them with a common waveform that is generally considered to be well known (basically, the shape of point sources is that of the beam) but with unknown positions and intensities, that are embedded in additive noise (not necessarily white). In the field of microwave Astronomy, wavelet techniques (Vielva et al. 2001, 2003; González-Nuevo et al. 2006; Sanz et al. 2006; López-Caniego et al. 2007), matched filters (MF, Tegmark & de Oliveira-Costa 1998; Barreiro et al. 2003; López-Caniego et al. 2006) and other related linear filtering techniques (Sanz et al. 2001; Chiang et al. 2002; Herranz et al. 2002,?; López-Caniego et al. 2004, 2005; López-Caniego et al. 2005) have proved to be useful. The common feature of all these techniques is that they rely on the prior knowledge that the sources have a distinctive spatial behaviour (i.e. a known spatial profile, plus the fact that they appear as compact objects as opposed to ‘diffuse’ random fields) that helps to distinguish them from the noise. Detection can be further improved by including prior information about the sources, i.e. some knowledge about their intensity distribution, in the frame of a Bayesian formalism (Hobson & McLachlan 2003; Carvalho et al. 2008).

Most of the current and planned CMB experiments are able to observe the sky at several wavelengths simultaneously. Multi-wavelength information makes it possible to separate different astrophysical components (as for example CMB from Galactic synchrotron emission) that have different spectral behaviour. Although multiwavelength component separation techniques have been very successful in separating diffuse components (for a recent comparative review of several methods applied to sky simulations very similar to the ones we will use in this paper, see Leach et al. 2008), the detection of EPS has been usually attempted on a channel by channel basis. The reason for this is that EPS form a very heterogeneous population, constituted by a large number of objects with very different physical properties, and therefore it is impossible to define a common spectral behaviour for all of them. The whole situation remains somewhat unsatisfactory: on the one hand, the channel-by-channel approach based on the spatial behaviour works fine, but a valuable fraction of the information that multi-wavelength experiments can offer is wasted this way. On the other hand, standard component separation techniques based on spectral diversity have problems when dealing with the very heterogeneous EPS components.

Thus, multi-wavelength detection of EPS in CMB images remains a largely unexplored field. In recent years, some attempts have been done in this direction. For example, Naselsky et al. (2002) combined simulated multi-wavelength maps in order to increase the average signal to noise ratio of point sources. In a similar way, Chen & Wright (2007) and Wright et al. (2008) use combinations of the *WMAP* W and V bands in order to produce a CMB-free map in which

to better detect the elusive radio galaxies. Note that, in any case, combined ‘clean’ maps are suitable for detecting more sources but not for performing accurate photometry, unless the spectral index of all the sources is known in advance.

An intermediate approach is to design filters that are able to find compact sources thanks to their distinctive spatial behaviour while at the same time do incorporate some multiwavelength information, without pretending to achieve a full component separation and without assuming a specific spectral behaviour for the sources. Very recently, the authors have proposed a new technique, based on the so-called ‘*matched matrix filters*’ (MTXF, Herranz & Sanz 2008), that goes in this direction. The basic underlying ideas of the new method are:

- When a source is found in one channel, it will be also present in the same position in all the other channels.
- The spatial profile of the sources may differ from channel to channel, but it is a priori known.
- The second order statistics of the background in which the sources are embedded is well known or it can be directly estimated from the data by assuming that point sources are sparse. This knowledge about the second order statistics (namely, the background’s power spectrum for each channel and the its correlations among the different channels) will be used to increase the signal to noise ratio of the sources.
- We want to perform accurate photometry of the sources at every one of the frequencies covered by the experiment, independently of what is the spectral behaviour of any source in particular.

In Herranz & Sanz (2008) the authors presented the new methodology and demonstrated its potential utility with a few toy simulations. In this paper, we will study its applicability to real CMB experiments by applying it to realistic simulations of the whole sky as will be observed by the upcoming *Planck* mission. We will focus on the particular case of the detection of radio sources in the four lower frequency *Planck* channels (33–100 GHz), comparing the performance of the new filters with the performance of the well-established standard matched filters. In section 2 we will summarize the foundations of the theoretical formulation of matched matrix filters. In section 3 we will describe the *Planck* simulations that we use to test the method and we will outline the main features of the code we have developed for its implementation. The results of the exercise will be commented in section 4. Finally, in section 5 we will draw some conclusions.

## 2 MATCHED MATRIX FILTERS

The derivation of the matched matrix filters is fully described in Herranz & Sanz (2008)<sup>1</sup>. However, for reasons of clarity, we will reproduce here the main ideas of that paper here.

### 2.1 Data model

Let us consider a set of  $N$  two-dimensional images (channels) in which there is an unknown number of point sources

<sup>1</sup> For economy, in the following we will occasionally refer to the matched matrix filters just as ‘matrix filters’

embedded in a mixture of instrumental noise and other astrophysical components. Without loss of generality, let us consider the case of a single point source located at the origin of the coordinates. Our data model is

$$D_k(\vec{x}) = s_k(\vec{x}) + n_k(\vec{x}), \quad (1)$$

where the subscript  $k = 1, \dots, N$  denotes the index of the image. The term  $s_k(\vec{x})$  denotes the point source,

$$s_k(\vec{x}) = A_k \tau_k(\vec{x}), \quad (2)$$

where  $A_k$  is the unknown amplitude of the source in the  $k^{\text{th}}$  channel and  $\tau_k(\vec{x})$  is the spatial profile of the source (which is assumed to be known) and satisfies the condition  $\tau_k(\vec{0}) = 1$ . The term  $n_k(\vec{x})$  in equation (1) is the generalized noise in the  $k^{\text{th}}$  channel, containing not only instrumental noise, but also CMB and all the other astrophysical components apart from the point sources. Let us suppose the noise term can be characterized by its cross-power spectrum:

$$\langle n_k(\vec{q}) n_l^*(\vec{q}') \rangle = P_{kl}(\vec{q}) \delta^2(\vec{q} - \vec{q}'), \quad (3)$$

where  $\mathbf{P} = (P_{kl})$  is the cross-power spectrum matrix and the symbol  $*$  denotes complex conjugation. From now on, we assume that the noise has zero mean:

$$\langle n_k(\vec{x}) \rangle = 0. \quad (4)$$

## 2.2 Filtering with matrices of filters

Since we are interested in doing accurate photometry in each one of the  $N$  available channels, we are bound to produce  $N$  different processed maps. Therefore, we are looking for a transformation that starts with  $N$  input channels and ends with other  $N$  processed maps where a) point sources are easier to detect and b) the amplitudes  $A_k$  are preserved. Besides, since we intend to use some multi-wavelength information, we are interested in making all the  $N$  input channels intervene in the elaboration of the any one of the output maps. One possibility is to define a set of  $N \times N$  filters  $\Psi_{kl}(\vec{x})$  such that the  $N$  combined quantities

$$\begin{aligned} w_k(\vec{x}) &= \sum_l \int d\vec{x}' \Psi_{kl}(\vec{x} - \vec{x}') D_l(\vec{x}') \\ &= \sum_l \int d\vec{q} e^{-i\vec{q} \cdot \vec{x}} \Psi_{kl}(\vec{q}) D_l(\vec{q}) \end{aligned} \quad (5)$$

are our processed maps. The last term of the equation is just the expression of the filterings in Fourier space, being  $\vec{q}$  the Fourier mode and  $\Psi_{lk}(\vec{q})$  and  $D_l(\vec{q})$  the Fourier transforms of  $\Psi_{kl}(\vec{x})$  and  $D_l(\vec{x})$ , respectively.

We intend to use the combined filtered image  $w_k(\vec{x})$  as an estimator of the source amplitudes  $A_k$  for all  $k = 1, \dots, N$ . Thus, the filters  $\Psi_{kl}$  must satisfy the condition that the  $k^{\text{th}}$  filtered, combined image at the position of the source is, on average over many realizations, an *unbiased* estimator of the amplitude of the  $k^{\text{th}}$  source. The other requirement we will ask the processed maps is that the signal to noise ratio of the sources is increased with respect to the input maps. In other words, we want estimators  $w_k$  to be not only unbiased, but *efficient* as well. Therefore, we need to minimize the variance  $\sigma_{w_k}$  of the combined filtered image.

The set of filters that minimize the variance  $\sigma_{w_k}$  for all  $k$  while keeping the individual amplitudes  $A_k$  constant for



**Figure 1.** Mask used for the analysis. The mask covers 14.91% of the sky, including the Galactic Plane plus some other densely contaminated areas of the sky such as the Magellanic Clouds, the Ophiuchus Complex and the Orion/Eridanus Bubble.

all the point sources, independently of their frequency dependence, can be shown to be given by the matrix equation:

$$\Psi^* = \mathbf{F} \mathbf{P}^{-1}, \quad (6)$$

where

$$\mathbf{F} = (F_{kl}), \quad \mathbf{P} = (P_{kl}), \quad \lambda = (\lambda_{kl}), \quad \mathbf{H} = (H_{kl}), \quad (7)$$

and where

$$\begin{aligned} F_{kl} &= \lambda_{kl} \tau_l, \\ \lambda &= \mathbf{H}^{-1}, \\ H_{kl} &= \int d\vec{q} \tau_k(\vec{q}) P_{kl}^{-1} \tau_l(\vec{q}). \end{aligned} \quad (8)$$

The set of filters we have developed naturally assume a structure that is best expressed in the form of a matrix equation, hence the denomination of ‘*matched matrix filters*’.

## 2.3 Properties of matched matrix filters and some particular cases

### 2.3.1 A single image

If the number of images is  $N = 1$  it is easy to show that the matrix of filters contains a single element, which is the complex conjugate of the standard matched filter. For circularly symmetric source profiles, the filter is real-valued and the resulting filter is exactly the same as the standard matched filter.

### 2.3.2 Uncorrelated noise

From equations (6) and (8) it is straightforward to show that for the particular case where the noise is totally uncorrelated among channels the matrix of filters defaults to a diagonal matrix whose non-zero elements are the complex conjugates of the standard matched filters that correspond to each input channel. When the source profiles are circularly symmetric the filters are real-valued and the whole process is equivalent to filter each channel independently with the appropriate matched filter.

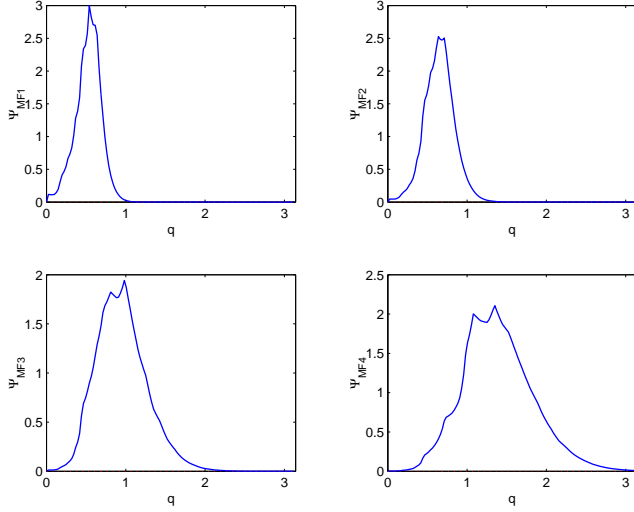


**Figure 2.** Standard matched filters, in Fourier space, for the four channels in one of the patches considered.

### 2.3.3 The $2 \times 2$ case

In this case, the explicit form of the MTXF is

$$\begin{aligned}
 \Psi_{11}^* &= \frac{1}{N\Delta} [\phi_1 - \phi_2 \frac{P_{12}b_{12}}{P_{11}b_{22}}], \\
 \Psi_{12}^* &= \frac{1}{N\Delta} [-\phi_1 \frac{P_{12}}{P_{22}} + \phi_2 \frac{b_{12}}{b_{11}}], \\
 \Psi_{22}^* &= \frac{1}{N\Delta} [\phi_2 - \phi_1 \frac{P_{12}b_{12}}{P_{22}b_{11}}], \\
 \Psi_{21}^* &= \frac{1}{N\Delta} [\phi_1 \frac{b_{12}}{b_{22}} - \phi_2 \frac{P_{12}}{P_{11}}], \\
 N &\equiv 1 - \frac{b_{12}^2}{b_{11}b_{22}}, \\
 \Delta &\equiv 1 - \frac{P_{12}^2}{P_{11}P_{22}}, \\
 b_{ij} &\equiv \int d\tilde{q} \frac{\tau_i \tau_j^*}{\Delta} \frac{P_{ij}}{P_{ii}P_{jj}},
 \end{aligned} \tag{9}$$

where  $i, j = 1, 2$  and  $\phi_i$  are closely related to the standard matched filters  $\phi_i^{MF}$ :

$$\begin{aligned}
 \phi_1 &= \frac{\tau_1}{b_{11}P_{11}} = \frac{c_1}{b_{11}} \phi_1^{MF}, \quad c_1 \equiv \int d\tilde{q} \frac{\tau_1^2}{P_{11}}, \\
 \phi_2 &= \frac{\tau_2}{b_{22}P_{22}} = \frac{c_2}{b_{22}} \phi_2^{MF}, \quad c_2 \equiv \int d\tilde{q} \frac{\tau_2^2}{P_{22}}.
 \end{aligned} \tag{10}$$

We remark that the MTXF is a non-symmetric matrix in general. The variances of the two filtered maps are

$$\begin{aligned}
 \sigma_{w1}^2 &= \frac{1}{Nb_{11}}, \\
 \sigma_{w2}^2 &= \frac{1}{Nb_{22}}.
 \end{aligned} \tag{11}$$

From the last equation, one obtains

$$\frac{\sigma_{w1}^2}{\sigma_{w2}^2} = \frac{b_{22}}{b_{11}}. \tag{12}$$

### 2.3.4 Relative gain of the different channels

An useful quantity that can be used to assess the performance of a filter is its *gain* factor, that is, the increment of the signal to noise ratio that a fiducial source experiments thanks to the application of a filter. Of course, gain is not a universal quantity of the filter, since it depends on the statistical properties of the background noise, but given a particular image the relative gain of two filters provides a good intuitive measurement of their respective performances. For unbiased filters (i.e. filters that preserve the amplitude of the signal) the gain is just the ratio of noise dispersions before and after filtering:

$$G = \frac{\sigma}{\sigma_w}, \tag{13}$$

where  $\sigma$  is the noise dispersion before filtering and  $\sigma_w$  is the noise dispersion after filtering.

When comparing the performances of matched matrix filters with those of standard matched filters, Herranz & Sanz (2008) observed an apparent trend: in all the few cases they studied, the gain factor of the matrix filters was similar to the one of matched filters for at least one of the channels, and significantly higher for the others. Moreover, the channel with the lower gain was the one with the worse signal to noise ratio after filtering. At the moment, it was not clear if this was a universal trend of just a result obtained by chance given the low number of cases under studied in that work. As we will see below, the results of this work seem to support this observed trend.

There is a qualitative argument that sheds light over this phenomenon: for the sake of simplicity let us consider two channels and identical profiles  $\tau_1 = \tau_2$ . If one assumes that  $P_{11} < P_{22}$  then the equations (10,11) lead to

$$\sigma_{w1} < \sigma_{w2}, \quad \sigma_{w1}^{MF} < \sigma_{w2}^{MF}, \tag{14}$$

for the MTXF and standard MF, respectively. Therefore, the original map with less variance gains more with either filter. On the other hand, assuming that  $P_{12} \ll P_{11} < P_{22}$ , taking into account equations (10,11) and the Schwartz inequality, one obtains

$$\sigma_{w1} \leq \sigma_{w1}^{MF}, \tag{15}$$

i.e. the MTXF outperform the standard MF.

## 3 APPLICATION TO PLANCK RADIO SOURCES

In this section, we will describe an application of the new multiwavelength filtering technique to realistic simulations of the sky as it will be observed by the *Planck* mission. As a example, we will focus on the blind detection of extragalactic radio sources. Therefore we will simulate the 30, 44, 70 and 100 GHz *Planck* channels. Note that although a simultaneous multiwavelength filtering of the nine *Planck* channels is relatively easy to do (it would imply the use of a  $9 \times 9$  matrix of filters, that can be easily handled by any desktop computer), the addition of infrared channels would probably help little to the detection radio sources. A intuitive reason for this is that the sources that are bright in the infrared range are not necessarily the same that dominate the radio range, and vice versa. Therefore, for this work

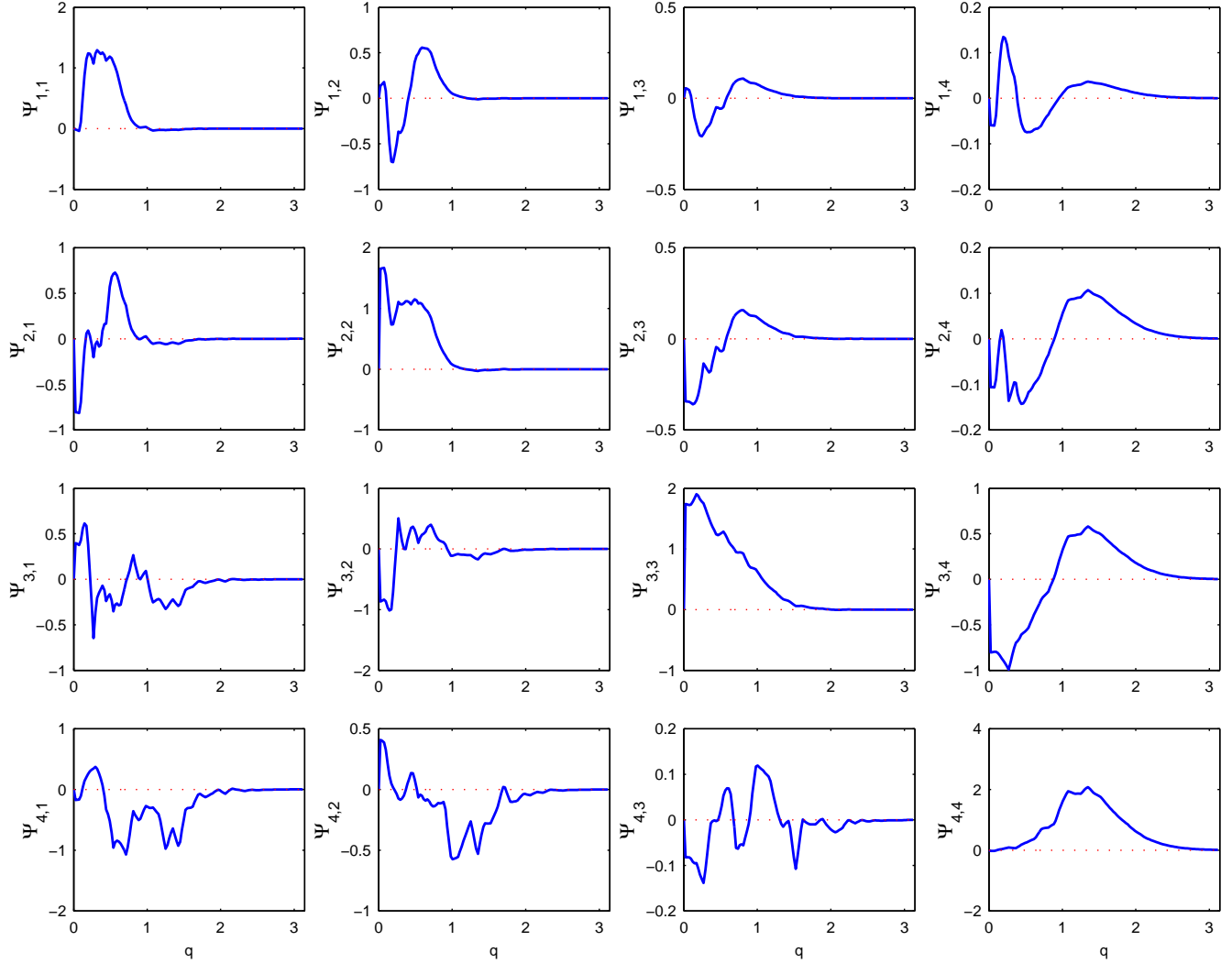


**Figure 3.** The different elements of the  $4 \times 4$  matrix of filters, in Fourier space, for the same patches as in figure 2.

we prefer to treat the radio sources separately. Besides, the low-dimensional  $4 \times 4$  application we describe here is more adequate to illustrate the technique, allowing us to show the details of the method with a relatively small number of plots.

### 3.1 The simulations

Sky simulations are based on the Planck Sky Model<sup>2</sup> (PSM, Delabrouille et al. 2008, in preparation), a flexible software package developed by Planck WG2 for making predictions, simulations and constrained realisations of the microwave sky.

The CMB sky is based on a Gaussian realisation assuming the WMAP best-fit  $C_\ell$  at higher multipoles.

The Galactic emission is described by a three component model of the interstellar medium comprising free-free, synchrotron and dust emissions. Free-free emission is based

on the model of Dickinson et al. (2003) assuming an electronic temperature of 7000 K. The spatial structure of the emission is estimated using a H $\alpha$  template corrected for dust extinction. Synchrotron emission is based on an extrapolation of the 408 MHz map of Haslam et al. (1982) from which an estimate of the free-free emission was removed. A limitation of this approach is that this synchrotron model also contains any dust anomalous emission seen by WMAP at 23 GHz. The thermal emission from interstellar dust is estimated using model 7 of Finkbeiner et al. (1999).

Point sources are modeled with two main categories: radio and infra-red. Simulated radio sources are based on the NVSS or SUMSS and GB6 or PMN catalogues. Measured fluxes at 1 and/or 4.85 GHz are extrapolated to PLANCK frequencies assuming a distribution in flat and steep populations. For each of these two populations, the spectral index is randomly drawn within a set of values compatible with the typical average and dispersion. Infrared sources are based on the IRAS catalogue, and modelled as dusty galaxies. In addition, the emission of a large number of blended infrared galaxies, not present individually in the IRAS catalogue, is simulated to model the Far In-

<sup>2</sup> [http://www.apc.univ-paris7.fr/APC\\_CS/Recherche/Adamis/PSM/psky-en.php](http://www.apc.univ-paris7.fr/APC_CS/Recherche/Adamis/PSM/psky-en.php)

frared Background (González-Nuevo et al. 2005). We also include in the model a map of thermal SZ spectral distortion from galaxy clusters, based on a cluster catalogue randomly drawn using a mass-function compatible with present-day observations.

### 3.2 The code

In this work we have used a code that reads in four all-sky FITS maps with HEALPix (Górski et al. 2005) resolution parameter NSIDE=1024, one per frequency between 30 and 100 GHz. Second, according to some parameters given in an input file, the code uses the CPACK libraries<sup>3</sup> to divide the sky in a sufficient number of overlapping flat patches such that the 100% of the sky is covered. In this pixelization scheme, we have produced 371 patches per frequency, 14.656 square degrees and  $256 \times 256$  pixels each. Then the code proceeds to run either the MF or the MTXF algorithms on every set of four patches corresponding to the same region in the sky. Afterwards, once the optimally filtered image has been produced, the code looks for maxima in it producing a subcatalogue of detections. Finally, a combined catalogue is produced, removing possible repetitions inside a 1 FWHM radius.

## 4 RESULTS

As described above, we have divided the sky into square flat patches by projecting the HEALPix (Górski et al. 2005) maps into the tangent plane at a set of coordinates that are regularly distributed on the sphere. For each resulting patch we have four square images, one per frequency channel (30, 44, 70 and 100 GHz). Then we have filtered simultaneously the four images with the filters (6) specifically calculated for that region of the sky. In parallel, we have filtered each one of the images separately with its corresponding matched filter. Therefore, for each input image we have two output filtered images, one obtained with the standard matched filter and other obtained by the matrix filters as in equation (5). Then we have applied the same thresholding detection criterion to the two cases: for any given filtered map, we have selected all the peaks that have at least three connected pixels with flux above a given number of times the  $\sigma$  level<sup>4</sup> of the filtered map. Unless otherwise noted, all the plots that will be shown in this section will refer to detections above the  $5\sigma$  detection threshold. The detections thus obtained for the different patches have been combined into a single whole-sky catalogs for each of the four frequency channels and the two filtering schemes.

Figure 1 shows the Galactic mask we apply for the analysis of the results. The mask is similar to the WMAP Kp2 mask and it covers a highly contaminated region around the Galactic plane plus a set of irregular areas that mask other highly contaminated areas of the sky such as the Magellanic Clouds, the Ophiuchus Complex and the Orion/Eridanus

Bubble. In total, we are masking 14.91% of the pixels of the sky.

### 4.1 Detail of a single patch

Before discussing the results for all the sky outside the mask just described above, let us illustrate the qualitative functioning of the filters taking as an example just one sky patch. In the first row of plots of figure 4 we show the aspect of sky in the first of the patches we have studied, centered in the Galactic North Pole. It is a region of the sky with a very low contamination from Galactic emission, with two point sources that are clearly visible to the naked eye (at least at 30 GHz), but many others are hidden amid the diffuse components. EPS alone are shown in the second row of plots of the figure.

Figure 2 shows the matched filters, in Fourier space, for the four different channels shown in figure 4. Figure 3 shows the 16 elements of the corresponding matrix of filters, also in Fourier space. Note that the filters in the diagonal look roughly similar to the matched filters whereas the off-diagonal elements are quite different. This can be intuitively explained in the following way: the diagonal element  $\Psi_{kk}$  is designed to produce a maximum contribution of the source profile  $\tau_k$  in the map  $D_k$  whereas the  $\Psi_{kl}$ ,  $l \neq k$  element is designed to produce a minimum contribution of the source profile  $\tau_l$  in the map  $D_k$ . This way the off-diagonal elements of the filtering contribute to reduce noise but do not introduce bias in the determination of the fluxes in the  $k^{\text{th}}$  map.

The third and fourth rows of figure 4 show the output filtered patches for the matched filter and the matrix filters, respectively. Note that for the 44 and 70 GHz channels the output matrix filtered maps look far cleaner than their matched filtered equivalents. For the 30 GHz channel the distinction is not so clear (the matrix filtered image looks cleaner, but some of the sources that are easily visible in the matched filtered image are apparently missing; we will see later that this is only a visual effect). Finally, for the 100 GHz channel both filtered images look practically identical.

The gain factors obtained for these images with the MTXF are [2.9, 3.8, 3.5, 2.8] for the [30, 44, 70, 100] GHz channels. The gain ratio between the MTXF and the MF are  $G_{MTXF}/G_{MF} = [1.38, 1.52, 1.49, 1.00]$  for the [30, 44, 70, 100] GHz channels. Thus, the MTXF-filtered image with lower gain (100 GHz) is the one that is more similar to the correspondent MF-filtered image. Besides, the 100 GHz map is the one with higher variance before filtering. We will see in the next section that the all-sky results confirm this rule.

### 4.2 All-sky results

We can use the knowledge on the input EPS we have simulated to control the quality of our catalogs in terms of number of true and false detections. The criterion we use to decide whether a detection is a true one or a false one is purely positional: an object of the catalog is considered a true detection if it is closer than a certain matching radius  $r$  of an input source and a false (spurious) detection otherwise. For this work we use a matching radius  $r = 2R_0$ , where  $R_0$  is the width of the Gaussian beam corresponding to the channel

<sup>3</sup> <http://astro.ic.ac.uk/~mortlock/cpack/>

<sup>4</sup> Where  $\sigma$  is the standard deviation of the filtered map, excluding the region of the borders of the image; note that this  $\sigma$  level corresponds to a different flux threshold for different filters and for different regions of the sky



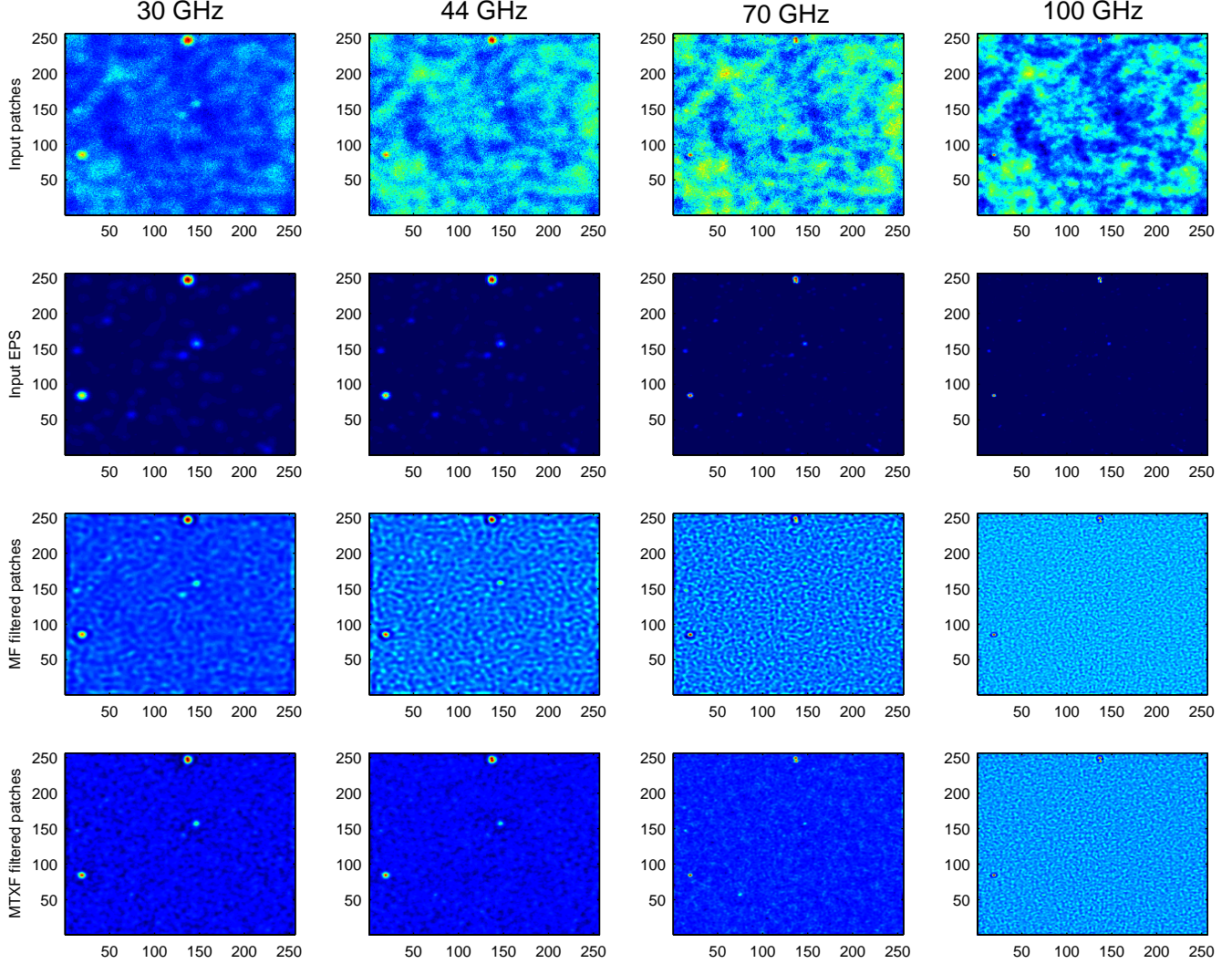


**Figure 4.** One of the regions of the sky. The patch is centered in the North Galactic Pole. The first row of images, starting from the top, shows the input patches at 30, 44, 70 and 100 GHz (from left to right of the figure). The second row of images shows separately the EPS contribution to the input maps, for the same frequencies. The third row shows the patches after having been filtered with the standard matched filter corresponding to each frequency. The bottom row shows the combined filtered maps resulting from the application of the matrix filters. All maps are expressed in MJy/sr units.

under study. This radius is smaller than one FWHM, so the criterion we use is quite stringent. Considerations about the flux matching will be made later in section 4.2.5.

#### 4.2.1 Number of detections

Figure 5 shows the number of detected sources in our  $5\sigma$  catalogs that have true fluxes  $S > S_0$ , as a function of the flux threshold  $S_0$ . The number of detections obtained with the MF is shown by a solid black line, whereas the number of detections obtained with the MTXF is shown by a dot-dashed blue line (colors are available only in the online version of the paper).

Two different cases can be observed: the 100 GHz channel and the other three channels. At the 100 GHz channel the performance of the two kinds of filters is almost identical. From 30 to 70 GHz and high and intermediate fluxes ( $\geq 0.6$  Jy) the two methods detect very similarly. The MTXF curve

runs slightly below the MF curve: the difference consists of a few high flux sources that are somehow missed by the MTXF. We will discuss this problem in more detail below.

In the low flux region of the plots the number of detected sources stop growing and the curves reach a plateau. The knee point of the curves roughly indicates the detection limit of the  $5\sigma$  catalogs. At 30, 44 and 70 GHz this turnover point occurs around 600 (400) mJy for the matched (matrix) filters. In other words, the MF reaches its detection limit at fluxes higher than the MTXF. Therefore the MTXF are able to go deeper and to detect many more faint sources than the MF. At 100 GHz both filters have their turnout points located around 400 mJy.

We have checked that the number of  $5\sigma$  detections obtained with the MF roughly agrees (taking into account the different sky coverage) with the results obtained in previous works (López-Caniego et al. 2006; Leach et al. 2008) that have made use of similar Planck simulations.

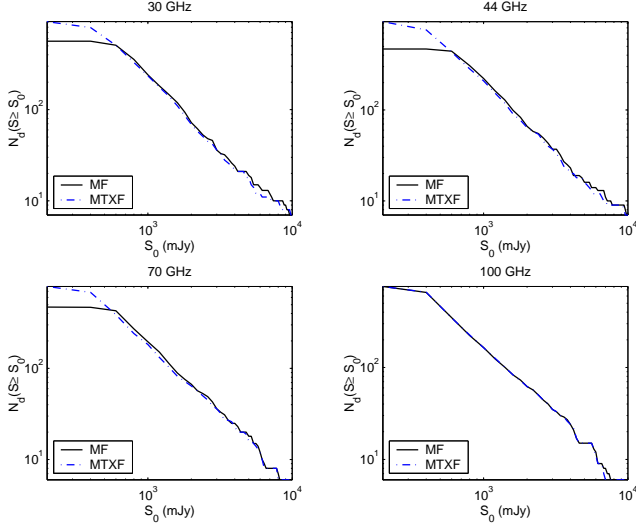


**Figure 5.** Number of true detections with true fluxes above a given flux value. Black solid line: detections with the matched filter. Blue dot-dashed line: detections with the matrix filters.

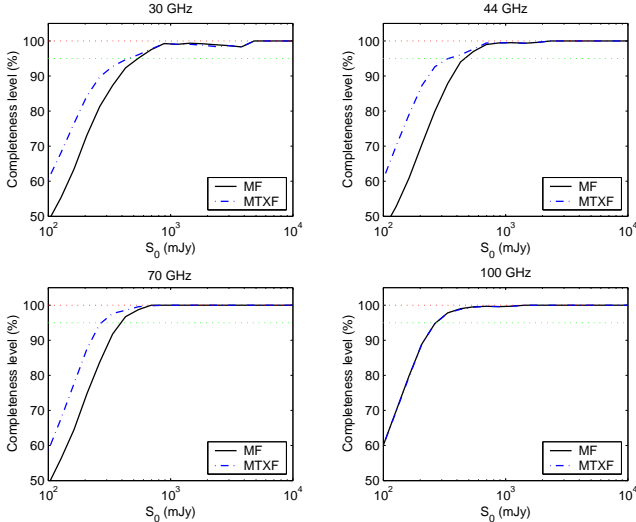


**Figure 6.** Completeness diagram. Black solid line: matched filter. Blue dashed line: matrix filters. The 100% and the 95% completeness levels are marked by a red dotted and a green dotted horizontal lines, respectively.

#### 4.2.2 Completeness

Figure 6 shows the completeness level as a function of the flux of the  $5\sigma$  catalogs obtained with the MF and the MTXF. Here the completeness is defined, as usual, as the ratio between the number of recovered true sources and the total number of input sources over a given flux limit. The 95% completeness level is marked by a horizontal green dotted line. The 95% completeness fluxes are, for the matched (matrix) filters, the following: at 30 GHz, 610 (540) mJy; at 44 GHz, 460 (340) mJy; at 70 GHz, 390 (270) mJy and, at 100 GHz, 270 (270) mJy. Three issues about figure 6 deserve detailed comments:

If compared to the data in Table 2 of López-Caniego et al. (2006), our present complete-

ness limits are higher than theirs. This is due to two causes: on the one hand, in this work we include regions of the sky that are closer to the Galactic plane and therefore more contaminated (and therefore, the  $5\sigma$  detection threshold corresponds to a higher flux), where it is more likely to loss some sources, and, on the other hand, our present detection/selection criterion requires to have peaks with at least three connected pixels. This more stringent criterion helps to reduce the number of spurious detections, but occasionally makes us loss some true sources as well.

Regarding the different channels, for the case of 30, 44 and 70 GHz the MTXF show a better completeness level at intermediate and low fluxes. This is because MTXF do amplify better the point source signal with respect to the foregrounds and therefore they can reach lower detection limits. At 100 GHz, both kinds of filtering lead to the same completeness levels.

Both methods do miss some bright sources, even at fluxes  $> 1$  Jy. For example, at 30 GHz both the MF and the MTXF fail to detect 4 sources with fluxes  $> 1$  Jy. Three of them are common for the two filters and in all the three cases are sources that are in heavily contaminated regions at low Galactic latitude, very close to the border of the mask. Apart from these three missing sources, the MF misses a source that is detected by the MTXF and the MTXF miss a source that is detected by the MF. The first one corresponds to a source close to the LMC and a few pixels away from our mask. The second case corresponds to a source that is 2.69 Jy source that is only 35 arcmin away from a detected 3.23 Jy source. Although the distance between both sources is slightly larger than the matching radius we used for this channel, the MTXF is unable in this case to resolve the two sources individually.

This suggest that the mask we have used is good enough to avoid most spurious detections, but it may be insufficient to guarantee completeness. Besides, a problem of blending with the MTXF arises when two high flux sources lie very close one to another. Although this situation is not frequent, this may explain the slight loss of performance of the MTXF in figure 5 for high and intermediate fluxes.

#### 4.2.3 Reliability

Another interesting indicator of the performance of the filters is the reliability of the catalogs obtained with them. Let it be  $N_d(\nu)$  the number of true detections above a certain detection threshold  $\nu$  and  $N_s(\nu)$  the number of spurious detections (false alarms) above the same threshold. Then we define the reliability in the usual way

$$r(\nu) = \frac{N_d(\nu)}{N_d(\nu) + N_s(\nu)}. \quad (16)$$

The reliability of our  $5\sigma$  catalogs is well above the 95% level for the two filtering schemes and the four channels we considered. In order to show the performance of the filter for lower reliability levels, in figure 7 we have gone deeper in the detection, down to the  $3\sigma$  level. The red dotted line in the figure 7 shows the  $r = 95\%$  reliability level. For the 30, 44 and 70 GHz channels the MTXF allow us to go to lower detection thresholds than the MF for a fixed required reliability level. For the 100 GHz channel the situation is the opposite, but the difference is small. Table 1 shows the



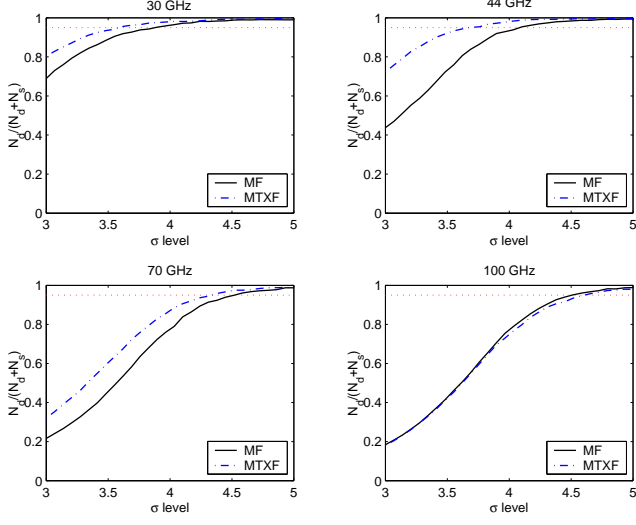


**Figure 7.** Reliability of the catalogs as a function of the limiting  $\sigma$  threshold for the two filters and the four channels. Black solid line: MF. Blue dot-dashed line: MTXF. The red dotted line shows the 95% reliability level.

threshold limits at the 95% reliability level and the corresponding number of true detections for the two filters and four channels considered. The improvement of the MTXF with respect to the MF is significant for the 30, 44 and 70 GHz channels.

#### 4.2.4 Receiver operating characteristics

Yet another way to comparatively study the performance of two detectors is the so-called *receiver operating characteristic* (ROC), or simply *ROC curve*. ROC curves are profusely used in detection theory because they provide a direct and natural way to relate the costs/benefits of the decision making associated to the detection process. Let us consider the two following quantities: the *true positives ratio* (TPR) is defined as

$$\text{TPR} = \frac{N_d}{NT}, \quad (17)$$

where, as before,  $N_d$  is the number of true detections (true positives) obtained for a certain detection threshold and  $NT$  is the total number of objects (in this case, simulated point sources) in the data set. The TPR is related, but not equivalent, to the completeness defined above (the number in the denominator of the completeness depends as well on the detection threshold, but  $NT$  does not).

The other quantity of interest is the spurious detection, false alarm or *false positive ratio* (FPR):

$$\text{FPR} = \frac{N_s}{FT}, \quad (18)$$

where  $N_s$  is defined as in section 4.2.3 and  $FT$  is the total number of candidates (in our case, peaks in the filtered images) that can be identified or not as ‘detections’ (true or false) by the detector. Therefore, there is an indirect relation between FPR and the reliability, but note that the quantity in the denominator in eq. (18) does not depend on the threshold. Both quantities, TPR and FPR, take values in

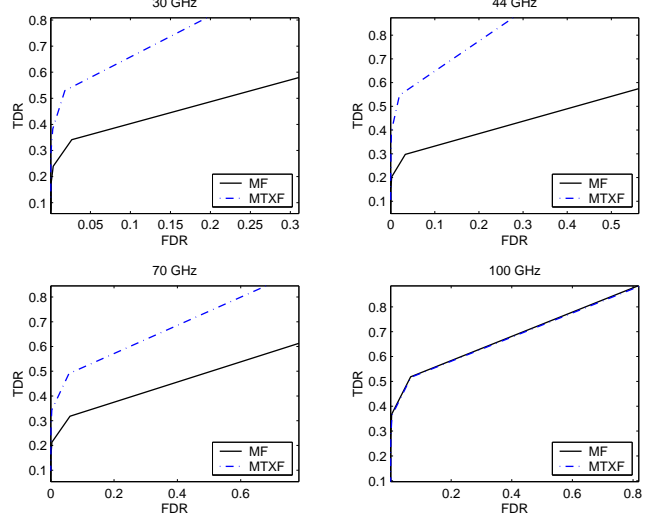


**Figure 8.** ROC curves for the filtering schemes and the four channels considered. Black solid line: matched filter. Blue dashed line: matrix filters.

the interval  $[0, 1]$  and they are called the *operating characteristics* of the detector. The TPR can be directly associated to the power of the detector and the FPR is related to its significance.

ROC curves are constructed by plotting the fraction of true positives (TPR) vs. the fraction of false alarms (FPR). They convey at a single glance the same information that can be found by taking together the figure 7 plus a set of tables akin to table 1 obtained at different reliability levels. For any fixed false alarm ratio the ROC curve tells the (normalized) number of true detections we have. ROC curves facilitate the comparison between two or more detectors (in our case, filters): the curve that lies above in the plot is closer to the optimal performance than the curves below.

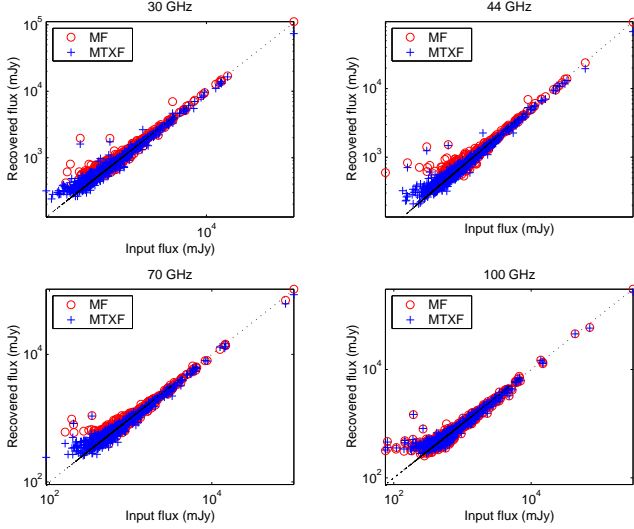
Figure 8 shows the ROC curves for the different cases and channels under consideration. The black solid line corresponds to the matched filter and the blue dashed line corresponds to the matrix filters (colors are available in the online version of the paper and on request to the authors). The number  $NT$  used for the plot is the total number of sources that are outside the masked area of the sky and that have fluxes above 150 mJy. The number  $FT$  is the total number of maxima found in the filtered images above the minimum considered threshold. The plots are made for  $\sigma$  detection thresholds in the interval  $\sigma \in [3, 10]$ . For this range of detection thresholds, the ROC curve corresponding to the matrix filters is clearly above the one corresponding to the matched filters for the 30, 44 and 70 GHz channels, meaning that if we fix any required spurious detection ratio we always have more true detections with the matrix filters than with the matched filters. For the 100 GHz channels the two curves run practically in parallel, but the matched filters are slightly above the matrix filters. This is related to the missing sources problem described in section 4.2.2.

#### 4.2.5 Flux estimation

Figure 9 shows how both kinds of filters do recover the fluxes of the sources in all the considered cases. Circles represent

**Table 1.** Threshold  $\sigma_{95\%}$  limit required for a 95% reliability, and corresponding number  $N_{d,95\%}$  of detections for such a threshold.

Frequency (GHz)	$\sigma_{95\%,MF}$	$N_{d,95\%,MF}$	$\sigma_{95\%,MTXF}$	$N_{d,95\%,MTXF}$
30	3.9	900	3.6	1600
44	4.1	705	3.7	1550
70	4.5	580	4.3	1000
100	4.5	940	4.6	895

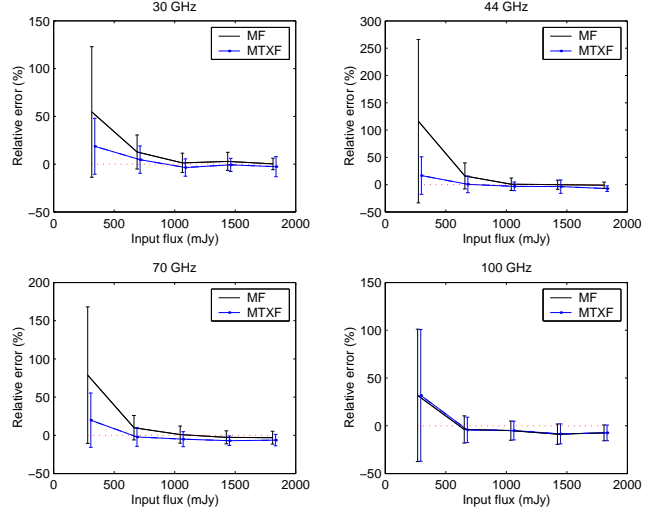
**Figure 9.** Estimation of the flux for the two filtering techniques. Red circles: matched filter estimation. Blue crosses: matrix filter estimation.

fluxes recovered with the MF and crosses represent fluxes recovered with the MTXF. There is an excellent agreement between true input and recovered fluxes for all the cases and between fluxes obtained with the MF and the MTXF. At low fluxes, the MF estimates show the well-known selection Eddington bias before than the MTXF. This is particularly evident at 44 and 70 GHz, but also visible at 30 GHz. As seen before, the MTXF filtered maps have less noise than the maps filtered with the MF and therefore the selection bias appears at a lower level. This also manifests in the smaller dispersion of blue crosses around the true value with respect to the red circles. However, for very high fluxes it seems that MTXF tends to underestimate the flux of the sources. At 100 GHz both filters lead to virtually the same results.

Figure 10 shows the relative flux error for the two filters and the four considered channels. We define the relative flux error as

$$e_{rel} = 100 \times \frac{\hat{S} - S_0}{S_0}, \quad (19)$$

where  $\hat{S}$  is the flux we estimate with the filters and  $S_0$  is the input flux. We take five flux bins between the flux of the faintest detected source and 2 Jy and for each bin we compute the average value and the dispersion of the relative error. The lowest bin is dominated by Eddington bias. This bias can be quite large, as is the case for the MF at 44 GHz (115% bias). The MTXF suffer less Eddington bias than the MF (except, as usual, for the 100 GHz case, where the two filters behave very similarly). As mentioned before, the

**Figure 10.** Relative flux estimation error and its dispersion. Black lines: matched filters. Blue solid line plus dots: matrix filters. For clarity, the lines corresponding to the matrix filter have been slightly displaced towards the right.

dispersion around the mean value is smaller for the MTXF. Finally, it is worth noticing the small negative bias suffered by both filters at high fluxes. This bias is not evident at 30 GHz, but it is easier to detect at higher frequencies. MTXF seem to be more biased (−6%, −6% and −8% at 44, 70 and 100 GHz, versus the MF biases that are −1%, −3% and −8% for the same frequencies). This kind of effect at high fluxes has been noticed before in related filtering applications (Herranz et al. 2002) and it is usually attributed to the non-ideality of the pixelized data, that makes imperfect the process of calculation of the normalization of the filters. In any case, the bias is relatively small and can be calibrated by means of simulations.

## 5 CONCLUSIONS

Although there is a relatively large number of works in the literature devoted to the detection of point sources in CMB images, there is practically no one that addresses the problem from the multi-frequency point of view. The reason is that each individual extragalactic point source has its own (a priori unknown) spectral behaviour and this makes it very hard to accommodate them in classic component separation schemes.

In this work we apply a novel linear filtering technique, the ‘*matched matrix filters*’, introduced by Herranz & Sanz (2008). Matched matrix filters incorporate full spatial information, including the cross-correlation among channels,

without making any a priori assumption about the spectral behaviour of the sources. The basic underlying idea is that in all the considered channels the sources do appear in the same unknown positions (but with different, unknown intensities) and have known spatial profiles given by the experiment point spread function, while some components of the background (i.e. CMB and Galactic emission) are correlated among channels. Then a clever linear filtering/combination of images can lead to a substantial reduction of the background, and therefore to lower source detection thresholds. The resulting expression of the filters takes form of a matrix given in terms of the cross-power spectra and the profile of the sources in the different maps.

We describe in detail the formalism of the matched matrix filters, looking in detail into some particular cases of interest, and we apply them to the detection of radio sources in realistic all-sky *Planck* simulations at 30, 44, 70 and 100 GHz. We use state-of-the-art simulations developed by the *Planck* WG2 Collaboration that include all the astrophysical components and instrumental specifications of the *Planck* mission. In order to tackle the strong non stationarity of the sky emission, we divide the sky into  $371\ 14.656 \times 14.656$  overlapping square degrees flat patches where we apply the two filtering techniques. For each patch and frequency we obtain a sub-catalog of detections. Then all the sub-catalogs corresponding to the same frequency are combined into an all-sky catalog. In order to compare with a well established mono-frequency approach, we repeat the same process using the standard matched filter.

We compare both methods in terms of reliability, completeness, receiver operating characteristics and flux accuracy. We find that for the three lower frequency channels (30, 44 and 70 GHz) the new matched matrix filters clearly outperform the standard matched filters for all these quality indicators. The matched matrix filters decrease significantly the noise level, what translates into a lower detection threshold and a reduced number of false detections. The flux estimation is consequently improved, with a lower dispersion around the true input value and a lower flux at which the well-know selection Eddington bias occur. The improvement is particularly evident at 44 GHz. At 100 GHz, however, the performance of the two filters is very similar. We indicate some possible reasons for this behavior, based on general analytical considerations about the structure of the filters.

One of the most interesting ways to compare two catalogs obtained with different methods is to set a fixed level of reliability, cut the catalogs at the corresponding points and compare how many detections there are in each of them. We find a noticeable increment of the number of true detections for a fixed reliability level obtained with the matched matrix filters with respect to the standard matched filters. In particular, for a 95% reliability we practically double the number of detections at 30, 44 and 70 GHz: the ratio between the number of detections obtained with the MTXF and the MF for these channels are 1.8, 2.2 and 1.7, respectively.

We would like to stress once more the importance of including multi-frequency information in this approach. The new matched multi-filters can be used to increase very significantly the number of extragalactic point source detections in upcoming CMB experiments such as *Planck* as well as in current experiments such as WMAP. A work on the

application of this technique to the 5 year WMAP data is in preparation.

Although here we have tested the MTXF to the particular case of the detection of radio sources in the low frequency channels of *Planck*, the same technique can be easily applied to other frequency bands, or to other fields of image analysis where pointlike objects appear in different frames (images).

## ACKNOWLEDGMENTS

The authors acknowledge partial financial support from the Spanish Ministry of Education (MEC) under project ESP2004-07067-C03-01 and from the joint CNR-CSIC research project 2006-IT-0037. MLC acknowledges the Spanish MEC for a postdoctoral fellowship. JLS acknowledges partial financial support by the Spanish MEC and thanks the CNR ISTI in Pisa for their hospitality during his sabbatical leave. Partial financial support for this research has been provided to JGN by the Italian ASI (contracts Planck LFI Activity of Phase E2 and I/016/07/0 ‘COFIS’) and MUR. We acknowledge the use of the HEALPix (Górski et al. 2005) code for all sphere-based computations. The authors acknowledge the use of the Planck Sky Model, developed by the Component Separation Working Group (WG2) of the *Planck* Collaboration.

## REFERENCES

- Barreiro R. B., Sanz J. L., Herranz D., Martínez-González E., 2003, MNRAS, 342, 119
- Bennett C. L., Bay M., Halpern M., Hinshaw G., Jackson C., Jarosik N., Kogut A., Limon M., Meyer S. S., Page L., Spergel D. N., Tucker G. S., Wilkinson D. T., Wollack E., Wright E. L., 2003, ApJ, 583, 1
- Carvalho P., Rocha G., Hobson M. P., 2008, ArXiv e-prints, 802
- Chen X., Wright E. L., 2007, ArXiv e-prints, 712
- Chiang L.-Y., Jørgensen H. E., Naselsky I. P., Naselsky P. D., Novikov I. D., Christensen P. R., 2002, MNRAS, 335, 1054
- de Zotti G., Ricci R., Mesa D., Silva L., Mazzotta P., Toffolatti L., González-Nuevo J., 2005, A&A, 431, 893
- de Zotti G., Toffolatti L., Argüeso F., Davies R. D., Mazzotta P., Partridge R. B., Smoot G. F., Vittorio N., 1999, in Maiani L., Melchiorri F., Vittorio N., eds, 3K cosmology Vol. 476 of American Institute of Physics Conference Series, The Planck Surveyor Mission: Astrophysical Prospects. pp 204–+
- Delabrouille et al. 2008, in preparation
- Dickinson C., Davies R. D., Davis R. J., 2003, MNRAS, 341, 369
- Finkbeiner D. P., Davis M., Schlegel D. J., 1999, ApJ, 524, 867
- González-Nuevo J., Argüeso F., López-Caniego M., Toffolatti L., Sanz J. L., Vielva P., Herranz D., 2006, MNRAS, 369, 1603
- González-Nuevo J., Toffolatti L., Argüeso F., 2005, ApJ, 621, 1

- Górski K. M., Hivon E., Banday A. J., Wandelt B. D., Hansen F. K., Reinecke M., Bartelmann M., 2005, *ApJ*, 622, 759
- Haslam C. G. T., Salter C. J., Stoffel H., Wilson W. E., 1982, *A&AS*, 47, 1
- Herranz D., Gallegos J., Sanz J. L., Martínez-González E., 2002, *MNRAS*, 334, 533
- Herranz D., Sanz J. L., 2008, submitted to the IEEE Journal on Selected Topics in Signal Processing
- Herranz D., Sanz J. L., Barreiro R. B., Martínez-González E., 2002, *ApJ*, 580, 610
- Hinshaw G., Nolte M. R., Bennett C. L., Bean R., Doré O., Greason M. R., Halpern M., Hill R. S., Jarosik N., Kogut A., Komatsu E., 2007, *ApJS*, 170, 288
- Hobson M. P., Barreiro R. B., Toffolatti L., Lasenby A. N., Sanz J., Jones A. W., Bouchet F. R., 1999, *MNRAS*, 306, 232
- Hobson M. P., McLachlan C., 2003, *MNRAS*, 338, 765
- Leach S. M., Cardoso J. F., Baccigalupi C., Barreiro R. B., Betoule M., Bobin J., Bonaldi A., de Zotti G., Delabrouille J., Dickinson C., 20 coauthors more 2008, *ArXiv e-prints*, 805
- López-Caniego M., González-Nuevo J., Herranz D., Mascardi M., Sanz J. L., De Zotti G., Toffolatti L., Argüeso F., 2007, *ApJS*, 170, 108
- López-Caniego M., Herranz D., Barreiro R. B., Sanz J. L., 2004, in Bouman C. A., Miller E. L., eds, *Computational Imaging II*. Edited by Bouman, Charles A.; Miller, Eric L. Proceedings of the SPIE, Volume 5299, pp. 145-154 (2004). Vol. 5299 of Presented at the Society of Photo-Optical Instrumentation Engineers (SPIE) Conference, A Bayesian approach to filter design: detection of compact sources. pp 145-154
- López-Caniego M., Herranz D., Barreiro R. B., Sanz J. L., 2005, *MNRAS*, 359, 993
- López-Caniego M., Herranz D., González-Nuevo J., Sanz J. L., Barreiro R. B., Vielva P., Argüeso F., Toffolatti L., 2006, *MNRAS*, 370, 2047
- López-Caniego M., Herranz D., Sanz J. L., Barreiro R. B., 2005, *EURASIP Journal on Applied Signal Processing*, 15, 2426
- Naselsky P., Novikov D., Silk J., 2002, *MNRAS*, 335, 550
- Sanz J. L., Herranz D., López-Caniego M., Argüeso F., 2006, in *Proceedings of the 14th European Signal Processing Conference (2006)*. *EUSIPCO 2006 Conference*, Wavelets on the sphere. Application to the detection problem. pp 1-5
- Sanz J. L., Herranz D., Martínez-González E., 2001, *ApJ*, 552, 484
- Tauber J. A., 2005, in Lasenby A. N., Wilkinson A., eds, *New Cosmological Data and the Values of the Fundamental Parameters* Vol. 201 of *IAU Symposium*, The Planck Mission. pp 86+
- Tegmark M., de Oliveira-Costa A., 1998, *ApJL*, 500, L83+
- The Planck Collaboration 2006, *ArXiv Astrophysics e-prints*
- Toffolatti L., Argüeso Gomez F., de Zotti G., Mazzei P., Franceschini A., Danese L., Burigana C., 1998, *MNRAS*, 297, 117
- Tucci M., Martínez-González E., Toffolatti L., González-Nuevo J., De Zotti G., 2004, *MNRAS*, 349, 1267
- Tucci M., Martínez-González E., Vielva P., Delabrouille J., 2005, *MNRAS*, 360, 935
- Vielva P., Barreiro R. B., Hobson M. P., Martínez-González E., Lasenby A. N., Sanz J. L., Toffolatti L., 2001, *MNRAS*, 328, 1
- Vielva P., Martínez-González E., Gallegos J. E., Toffolatti L., Sanz J. L., 2003, *MNRAS*, 344, 89
- Wright E. L., Chen X., Odegard N., Bennett C. L., Hill R. S., Hinshaw G., Jarosik N., Komatsu E., Nolte M. R., Page L., Spergel D. N., 2008, *ArXiv e-prints*, 803